Nanoscale analysis of the oxidation state and surface termination of praseodymium oxide ultrathin films on ruthenium(0001)

J.I. Flege[a,b,*], J.-O. Krisponeit[a,b], J. Höcker[a], M. Hoppe[a], Y. Niu[c], A. Zakharov[c], A. Schaefer[d], J. Falta[a,b], E. E. Krasovskii[e,f,g]

[a] *Institute of Solid State Physics, University of Bremen, Otto-Hahn-Allee 1, 28359 Bremen, Germany*
[b] *MAPEX Center for Materials and Processes, University of Bremen, 28359 Bremen, Germany*
[c] *MAX IV Laboratory, Box 118, 221 00 Lund, Sweden*
[d] *Division of Synchrotron Radiation Research, Lund University, 221 00 Lund, Sweden*
[e] *Departamento de Física de Materiales, Universidad del Pais Vasco UPV/EHU, 20080 San Sebastián/Donostia, Basque Country, Spain*
[f] *Donostia International Physics Center (DIPC), 20018 San Sebastián/Donostia, Basque Country, Spain*
[g] *IKERBASQUE, Basque Foundation for Science, 48013 Bilbao, Spain*

Abstract

The complex structure and morphology of ultrathin praseodymia films deposited on a ruthenium(0001) single crystal substrate by reactive molecular beam epitaxy is analyzed by intensity-voltage low-energy electron microscopy in combination with theoretical calculations within an *ab initio* scattering theory. A rich coexistence of various nanoscale crystalline surface structures is identified for the as-grown samples, notably comprising two distinct oxygen-terminated hexagonal $Pr_2O_3(0001)$ surface phases as well as a cubic $Pr_2O_3(111)$ and a fluorite $PrO_2(111)$ surface component. Furthermore, scattering theory reveals a striking similarity between the electron reflectivity spectra of praseodymia and ceria due to very efficient screening of the nuclear charge by the extra $4f$ electron in the former case.

Keywords: praseodymia, ceria, low-energy electron microscopy and diffraction, oxide films, rare-earth oxides, electron scattering

1. Introduction

Metal oxide surfaces and thin films are almost ubiquitously found in solid state nanoscience and technology, ranging from applications in microelectronics as integral parts of field effect transistors in complementary metal-oxide-semiconductor technology to functional coatings in tribology and sensing as well as active support materials in heterogeneous catalysis. To determine their specific role in any of these fields of application, a detailed understanding of the fundamental structural (geometric) properties of the oxide films is key to understanding their physical, chemical, and materials properties, which in turn govern their interaction with their surrounding or give rise to their specific funtionality. Owing to the structural heterogeneity that is frequently found in the materials employed, a microscopic approach to unraveling the (local) structure and spatial distribution of the oxide is often required. This is even more so when the problem demands a description on different length scales, e. g., of the elemental interactions on an atomic scale and diffusive processes over mesoscopic to macroscopic distances, which is a situation typically encountered in heterogeneous catalysis.

Low-energy electron microscopy (LEEM) [1] is a surface science technique that combines full-field diffractive imaging with ultrahigh vacuum compatibility and surface sensitivity. The latter is ensured by using slow electrons impinging on the sample surface typically at normal incidence and kinetic energies from about 0 eV up to a few tens of eV, which depending on electron energy, geometric and electronic structure gives rise to strongly backscattered electron beams [2]. Owing to the diffractive nature of the electron-sample interaction and the underly-

*Corresponding author
Email address: flege@ifp.uni-bremen.de (J.I. Flege)

ing scattering processes, the energy-dependent reflected beam intensity, i. e., the so-called intensity-voltage ($I(V)$) curve of the (00) beam in conventional low-energy electron diffraction (LEED) nomenclature, may comprise intensity modulations that are characteristic of the illuminated material and its particular geometric and electronic structure [3]. The dependence on surface geometric and electronic structure has also been shown for the related, earlier developed very-low-energy electron diffraction (VLEED) technique and also found in theoretical approaches to understand the problem of electron reflectance spectra from crystalline surfaces [4–7]. Consequently, in bright-field imaging mode this $I(V)$ dependence determines the local electron reflectivity and represents the corner stone of amplitude contrast formation for heterogeneous samples.

A few years ago, we have demonstrated that local $I(V)$ analysis performed in bright-field LEEM is capable of identifying the structure of atomically thin transition metal oxide films, e. g., of NiO [8] and few-nanometer thin films of cerium oxide of different oxidation state [9–11]. Local $I(V)$ analysis has also been employed in a fingerprinting mode to distinguish between various forms of iron oxide [12–15]. Yet, due to an extended probing depth at very low electron energies a rather contentious topic is the question whether $I(V)$-LEEM is also able to distinguish between different terminations of the oxide, which may possibly coexist after preparation in addition to different oxidation states. Recently, we have provided evidence that $I(V)$-LEEM is able to discriminate between various submonolayer coverages between one quarter to a full monolayer of chemisorbed oxygen on Ru(0001) [16].

Here, we analyze the reflectivity spectra of ultrathin praseodymium oxide films grown on a Ru(0001) surface, which we have very recently shown to initially form large, regular shaped oxide islands that sequentially thicken in a layer-by-layer fashion at a later stage [17]. We showcase that, in perfect analogy to cerium oxide [10], we can distinguish between the different crystallographic structures (hexagonal (a)-Pr_2O_3, cubic (c)-Pr_2O_3, and (fluorite) PrO_2) representative of the different valence states (Pr^{3+}, Pr^{4+}) for the praseodymium cations [18], and we will show that our method even allows distinguishing and determining the local type of oxide termination within the same oxidation state and crystal structure.

2. Material and methods

The experiments were performed in two separate commercial Elmitec LEEM III systems, one installed at the University of Bremen, Germany and the other at beamline I311 of the MAX-lab synchrotron radiation facility in Lund, Sweden. The latter system is additionally equipped with an energy filter enabling operation as a spectroscopic photoemission and low-energy electron microscope (SPE-LEEM), employing low energy electrons from the internal electron gun or photoelectrons excited by the incident synchrotron radiation in a photon energy range of about 43-1500 eV. Both operation modes have been used for extensive characterization of the praseodymia growth on Ru(0001) in a previous study [17]. Briefly, the Ru(0001) single crystal (Mateck) was cleaned *in situ* using established procedures, involving repeated oxidation and high-temperature annealing as described elsewhere [19, 20]. Sequentially, praseodymium oxide was deposited *in situ* by reactive molecular beam epitaxy (MBE) involving evaporation of metallic Pr onto the clean Ru(0001) substrate at 760 °C in a molecular oxygen partial pressure of 5×10^{-7} Torr. Oxide island thicknesses were determined by *ex situ* atomic force microscopy (AFM).

In the present article, we concentrate on the detailed analysis of the accompanying $I(V)$-LEEM data that were acquired for the same samples as presented in the growth study [17]. In contrast to previous $I(V)$-LEEM studies of similar systems, the $I(V)$ curves were collected with an energy slit in the dispersive plane of the energy analyzer of the microscope in Lund (effective energy resolution about 0.3 eV), resulting in enhanced image contrast and visibly sharper features in the $I(V)$ spectra than in our LEEM III system without energy filter. While both effects are most prominent at very low energies, e. g., near the transition to the mirror mode, the main part of the $I(V)$ curve is only weakly affected.

3. Results and Discussion

This section is organized as follows: In Sec. 3.1, we present characteristic $I(V)$ curves for flat praseodymia films and recap important results from the previous growth study [17], thereby introducing the most prominent crystallographic structures of bulk praseodymia. The theoretical methodology for the calculation and interpretation of the electron

reflectivity spectra of praseodymia surfaces is laid out in Sec. 3.2, which also includes a comparison to ceria, the neighboring lanthanide. The following Sec.3.3 is devoted to the comparison between calculated spectra and experimentally available data, facilitating an identification of the distinct structural components of the oxide film. Finally, based on the structural identification obtained, we apply the $I(V)$-LEEM fingerprinting methodology to obtain a quantitative mapping of the praseodymia surface composition with spatial resolution in the low nanometer range (Sec 3.4) and discuss the structural implications for the praseodymia-ruthenium system.

3.1. Intensity-voltage analysis of praseodymia films on Ru(0001)

A representative LEEM image of the praseodymia film grown on the Ru(0001) surface is displayed in Fig. 1(a). From the *in situ* observations during growth [17] in combination with spatially resolved X-ray absorption spectroscopy (XAS) data recorded in photoemission electron microscopy (XAS-PEEM) mode, the bright regions were attributed to substrate regions that are not covered by praseodymia. The oxide islands have evolved along the substrate steps and step bunches, which run from the top toward the bottom edge of the image. Yet, $I(V)$ analysis readily reveals these surface regions to be composed of a chemisorbed monolayer of oxygen within a (1×1)-O structure [16, 20]. However, the areas attributed to the praseodymia islands exhibit *five* distinct $I(V)$ curves as shown in Fig. 1(b), which is indicative of a non-homogeneous composition of the oxide film. To enable a structural interpretation of the $I(V)$ data, the present state of knowledge for praseodymia growth on ruthenium will briefly be summarized.

In the previous study [17], based on XAS-PEEM, the oxidation state of the praseodymia islands was largely identified as Pr^{3+} whereas a substantial contribution of Pr^{4+}, which is representative of the fluorite crystal structure (see Fig. 2(a)), was discarded. Furthermore, together with micro-illumination low-energy electron diffraction (μLEED) the associated crystal structure was identified as the hexagonal sesquioxide $Pr_2O_3(0001)$ with two different registries to the underlying ruthenium, one in which the surface lattice is collinear with the substrate lattice (only found for in highly stepped substrate regions) and one in which the surface lattice is azimuthally rotated by ±11.5°. The existence of the c-Pr_2O_3 phase, also known as the bixbyite structure, was ruled out due to the absence of the closely spaced diffraction spots representative of the (4×4) surface periodicity with respect to the fluorite structure (cf. Fig. 2(b) for details). Moreover, the contrast observed in dark-field LEEM using the praseodymia integer beams was tentatively

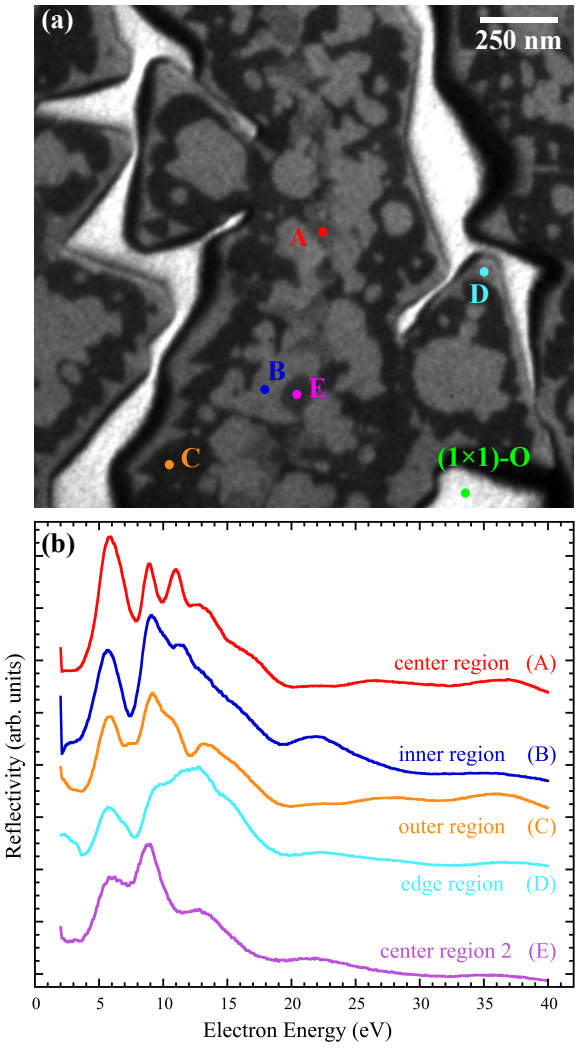

Figure 1: $I(V)$-LEEM analysis of praseodymia grown on Ru(0001). (a) LEEM image recorded at an electron kinetic energy of 12.1 eV. The different oxide components are labeled. The bright regions between the praseodymia are readily identified as chemisorbed oxygen within a (1×1)-O structure. (b) $I(V)$ fingerprints representing the different praseodymia regions. The nature of the individual regions "A" to "E" is identified in Fig. 4.

explained by the existence of two different surface terminations of the $Pr_2O_3(0001)$ film separated by an atomic step about 3 Å high, which corresponds to half the height of the bulk unit cell of the hexagonal crystal structure. Moreover, the six-fold symmetry of the bulk is broken at the surface, as also illustrated in Fig. 2(c).

Due to the structural similarity between the two lanthanides cerium oxide and praseodymium oxide, it is quite reasonable to approach the problem of $I(V)$ analysis for praseodymia by comparing to the known $I(V)$ curves for cerium oxide, which are already quite well understood based on calculation using *ab initio* scattering theory [10]. Intriguingly, closer inspection of Fig. 1(b) indeed reveals a striking similarity between the $I(V)$ curve associated with the praseodymia island edges and the $I(V)$ spectrum from fully oxidized, highly ordered ceria, i. e., CeO_2, that has crystallized in the fluorite structure and with (111) orientation [9]. Likewise, the $I(V)$ curve representing the region labeled "center 2" strongly resembles the reflectivity spectrum previously assigned to fully reduced, cubic cerium oxide, i. e., c-$Ce_2O_3(111)$, exhibiting the bixbyite crystal structure [11]. Therefore, in the following we will address the problem of understanding image contrast observed in bright-field LEEM by an *ab initio* treatment of the electron scattering and reflection from bulk-terminated praseodymia surfaces, and we will compare the results with previous calculations for cerium oxide. Although we deal with ultrathin films with thicknesses in the order of a few nanometers or below, we will show that this approximation already gives good agreement with the experimental data, facilitating an identification of the individual sample regions.

3.2. Theory of VLEED from praseodymia surfaces

We will now analyze the electron reflectivity $R(E)$ of the cubic fluorite $PrO_2(111)$ and hexagonal $Pr_2O_3(0001)$ surfaces based on an *ab initio* scattering theory.

The reflectivity spectra are obtained by solving the Schrödinger equation for the scattering of a plane wave incident from the vacuum. The electron potential in the crystal half-space is taken to be the self-consistent one-particle potential of the density functional theory in the local density approximation (LDA). In the surface atomic layers the potential is different from the bulk; there it is calculated as a potential of a finite-thickness slab.

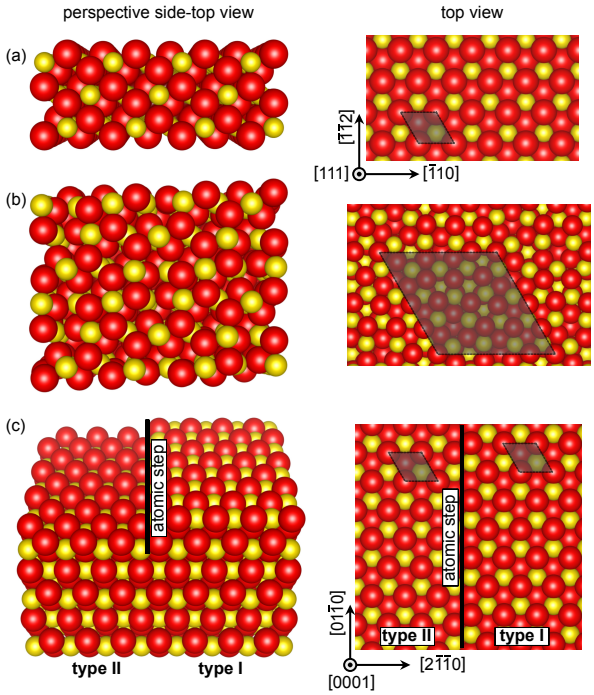

Figure 2: Crystal structures for praseodymia surfaces: (a) fluorite structure (PrO_2) consisting of a stack of O–Pr–O trilayers, (b) (cubic) c-Pr_2O_3 (bixbyite) structure, and (c) (hexagonal) a-Pr_2O_3 with different oxygen terminations "type I" and "type II", which are separated by an atomic step of about $c/2$. In each case, the unit mesh is highlighted.

In the inner layers of the slab the potential distribution coincides (with a certain accuracy) with that in the bulk, so the selvage is represented by a fragment of the slab, which is embedded between the semi-infinite bulk and vacuum, see a detailed description of the methodology in Ref. [8]. In the vacuum, the scattering wave function – the LEED state – is given in terms of plane waves, and in the bulk it is a linear combination of Bloch solutions [see Fig. 3(a)], with the two representations being smoothly continuously connected across the selvage region by a variational solution [21]. Thus, the elastic scattering is treated fully *ab initio*, with both the bulk band structure and the potential at the surface being realistic. The inelastic scattering is described by the optical potential – the energy dependent imaginary potential $-iV_i$, which is spatially constant in the crystal and zero in the vacuum half-space. The crystal structure is not adjusted to the experimental spectrum, and the relaxation of the surface layers is neglected, i. e., the bulk geometry is assumed to hold right up to the surface.

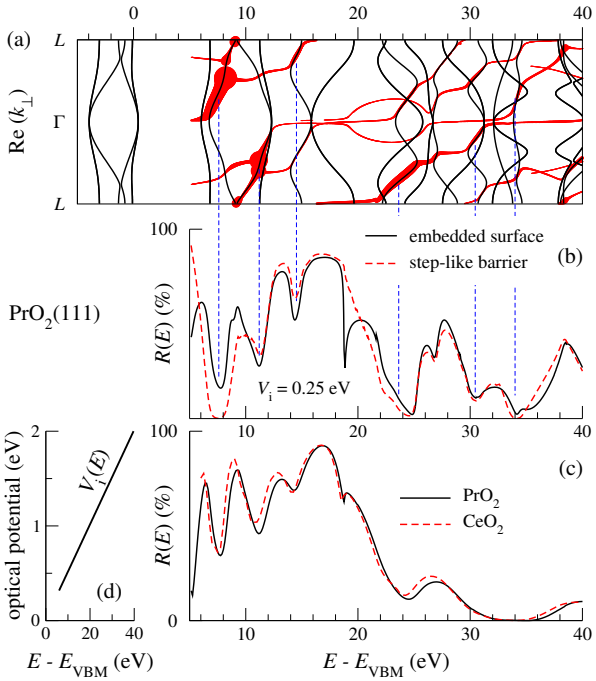

Figure 3: (a) Black lines show the real band structure of $PrO_2(111)$ for $\mathbf{k}_\parallel = 0$. Energies are relative to the valence band maximum E_{VBM}. Red lines of variable thickness indicate the Bloch waves that transmit the incident current into the bulk of the crystal (the thickness is proportional to the current transmitted by the individual partial wave). Note that only the waves that travel inside the crystal (and, thus, have the same sign of the group velocity) enter the LEED state. (b) Electron reflectivity $R(E)$ of the $PrO_2(111)$ surface calculated with $V_i = 0.25$ eV. The solid line is obtained with the embedding method [21], and the dashed line is obtained with a step-like surface barrier, i. e., the selvage is reduced to zero. The vertical dashed lines show the relation of the $R(E)$ minima to conducting fragments of the complex band structure. (c) Theoretical $R(E)$ for $PrO_2(111)$ (solid line) and for $CeO_2(111)$ [10] (dashed line) calculated with a linearly growing optical potential shown in graph (d).

Similar to ceria [10], the main problem in calculating the electronic structure of praseodymia stems from the partially occupied $4f$ shell, which is poorly described within a one-particle approach. In the fluorite CeO_2 the $4f$ band within the LDA is unoccupied, as is the case in reality, so the $4f$ electron does not participate in screening the nucleus. In Ref. [10], the theoretical $R(E)$ spectra of $CeO_2(111)$ were found to agree well with the experimental $I(V)$ curves. PrO_2 has an extra $4f$ electron per unit cell, and in the present calculation it was included into the ion core configuration, i. e., its density was taken to be the same as in the free atom, and the $4f$ band of Kohn-Sham eigenvalues remained unoccupied. The extra charge of the nucleus (relative to Ce) turns out to be perfectly screened, so that the calculated $R(E)$ curves for PrO_2 and CeO_2 are virtually identical, see Fig. 3(c). We note that the same similarity between ceria and praseodymia is observed for all the crystal structures considered (calculations not shown), with important implications in terms of structural identification.

In order to relate the minima in the $R(E)$ curve with the current-carrying Bloch states, we show in Fig. 3(b) the electron reflectivity for a physically negligible absorbing potential $V_i = 0.25$ eV. Almost everywhere the interpretation of the spectrum is quite straightforward: the $R(E)$ minima correspond to the appearance of propagating Bloch states, and the broad reflectivity maxima at $E - E_{VBM} = 17$ and 28 eV are due to band gaps: the Bloch states present in these gaps do not enter the LEED state. However, the low-energy maximum at 10 eV is not caused by a gap: it originates from a rapidly changing character of the conducting band. Figure 3(b) also tells us that in the present case the accurate treatment of the surface barrier is not very crucial for the gross features of electron reflection: the smooth potential barrier yields basically the same result as a step-like barrier, where the bulk crystal abruptly transfers into the vacuum.

3.3. Identification of surface components by $I(V)$ analysis

After theoretically establishing the striking analogy between the reflectivity spectra of ceria and praseodymia, we turn to the identification of the experimental curves from Fig. 1(b) and discuss the structural consequences.

A comparison between the five experimental $I(V)$ spectra and their theoretical counterparts is displayed in Fig. 4. The shape of the $I(V)$ curve associated with the edge region is very well reproduced by the calculated spectrum for $PrO_2(111)$. This observation clearly shows that the island rims, which based on AFM analysis are just a few O–Pr–O trilayers thin [17], indeed exhibit a higher oxidation state than the central parts of the islands. This surprising finding may be interpreted as evidence for the influence of the substrate, which possibly mediates a more effective charge transfer to the substrate and that may thereby stabilize a higher oxygen concentration in its vicinity. In addition, the (1×1)-O adsorbate layer may act as a reservoir for oxygen, thus facilitating O diffusion and spillover from the substrate to the oxide film at the elevated growth

temperature. We note that a single $PrO_2(111)$ trilayer film is virtually indistinguishable from a slab of a-$Pr_2O_3(0001)$ that is just half a unit cell thin. This fact may also serve to explain the occurrence of a fluorite-like PrO_2 trilayer in the thinnest regions of the praseodymia film.

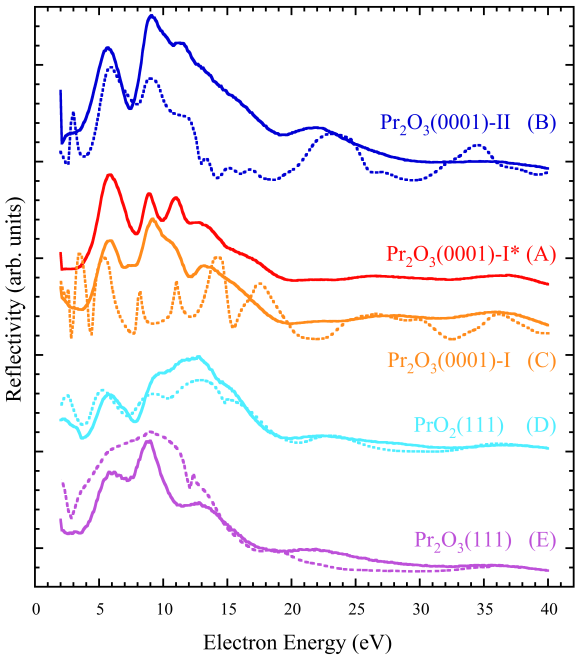

Figure 4: Comparison between experimental $I(V)$ spectra (solid lines) and theoretical reflectivity curves (dashed lines). The edge regions are identified as $PrO_2(111)$, the outer and inner island parts as oxygen-terminated a-$Pr_2O_3(0001)$ of types "I" and "II", respectively. One of the thicker, center regions matches the c-$Pr_2O_3(111)$ structure, the other is tentatively attributed to a variation of termination "I".

The center region 2 ("E") is rather successfully reproduced by the theoretical spectrum obtained for the cubic bixbyite-like structure, i. e., c-$Pr_2O_3(111)$, adding to the nanoscale heterogeneity of the surface. Furthermore, the two curves representing the so-called inner and outer parts of the praseodymia islands are tentatively identified and tied to the two oxygen-terminated surfaces of a-$Pr_2O_3(0001)$ as illustrated in Fig. 2(c), in accordance with the μLEED and dark-field LEEM interpretation of the previous study [17]. The center region ("A") and the outer region ("C") are seen to better match the spectrum representing termination "I". The slight deviation between the curves suggests that the difference most likely originates from the different thicknesses of these central and outer parts, possibly concomitant with different amounts of strain relaxation and the occurrence of slight variations in reconstruction. Finally, the spectrum of the inner region is attributed to the termination "II"; hence, every change from dark to bright within the islands can be explained by a change in surface structure after crossing an atomic step separating two distinct oxygen terminations of the a-$Pr_2O_3(0001)$ surface, in agreement with the structure model depicted in Fig. 2(c).

3.4. Mapping of surface components by two-dimensional $I(V)$-LEEM analysis

In this section, we apply $I(V)$-LEEM to achieve a structural and chemical mapping of the surface composition on the few nanometer scale. For this purpose, we use the $I(V)$ curves from the previous identification as fingerprints for the individual surface structures. A quantitative comparison is performed by systematically calculating the correlation coefficient between the local $I(V)$ curve and each spectrum from the set of reference $I(V)$ curves in a pixel-by-pixel fashion. Numerically, positive identification is achieved if the correlation coefficient is larger than or equal to a typical threshold level of the order of about 0.95, which from a statistical point of view means that the coefficient of determination amounts to about 0.90. Apart from its mathematical significance, the applicability of correlation analysis and the usefulness of this particular critical value as a first guess have also been determined and verified empirically for a large set of experimental $I(V)$-LEEM test data from various metal oxides and adsorbate systems [22]. For improved identification, depending on the particular system this threshold value may be optimized in a second step of the analysis.

In Fig. 5(a) a false-color map is presented that details the surface composition of the praseodymia film after the initial growth of the oxide by reactive MBE. From the $I(V)$ fingerprinting analysis, essentially all praseodymia regions depicted in the original bright-field LEEM image of Fig. 5(b) are successfully identified as one of the five phases labeled $PrO_2(111)$, c-$Pr_2O_3(111)$, a-$Pr_2O_3(0001)$-I, a-$Pr_2O_3(0001)$-II, and "praseodymia (center)". The black regions do not meet the rather strict criterion of a correlation threshold of 0.973 due to discrepancies mostly in the near-mirror electron mode range; however, in accordance with XAS-PEEM they can almost entirely be attributed to (1×1)-O reconstructed regions of the substrate. A

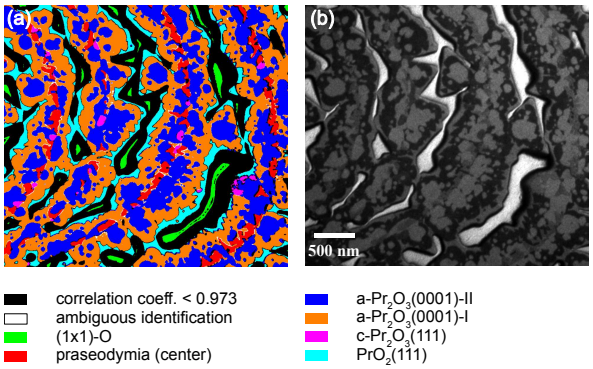

Figure 5: Mapping of local atomic structure by $I(V)$-LEEM fingerprinting with experimental $I(V)$ reference spectra. (a) False-color map indicating the local surface structure for every image pixel. Relatively large parts of the (1×1)-O regions appear black owing to a correlation coefficient slightly lower than the chosen threshold value (0.973). (b) Original bright-field LEEM image that includes the surface area shown in Fig. 1(a) for comparison (electron energy: 12.1 eV).

quantitative analysis of the false-color image composition from Fig. 5(a) yields the following relative phase-specific coverages: 2.0% (1×1)-O (without the black regions), 6.8% praseodymia (center), 42.1% a-Pr_2O_3(0001)-I, 37.8% a-Pr_2O_3(0001)-II, 1.1% c-Pr_2O_3(111), and 10.2% PrO_2(111). We note that a locally higher Ru step density leads to a higher structural heterogeneity and may also affect the relative abundance of the surface components.

From a methodological point of view, ensuring applicability and highest performance of the method demand a relatively high quality of the recorded $I(V)$ curves. Technically, apart from achieving a high lateral resolution this means that image drift due to residual thermal movement or misalignment of the sample and electron beam tilts should be avoided even if these deficiencies may be largely amended during post-processing; also a high signal-to-noise level is required for robust statistical correlation analysis. In the present case, the spatial resolution during the $I(V)$ measurement has been determined to 9.0 nm using the established 20%-80% criterion, which is seen to essentially translate into the fingerprinting analysis. Together with the work of Hannon and coworkers, who published a comparable value for an analysis performed of a bimetallic surface alloy [23], this is the highest spatial resolution achieved in $I(V)$-LEEM fingerprinting to date.

4. Conclusions

We have presented an extensive $I(V)$-LEEM analysis of the complex structure and morphology of ultrathin praseodymia films deposited on a ruthenium(0001) single crystal substrate. By analyzing the experimental electron reflectivity data within a numerical procedure, characteristic $I(V)$ spectra are determined, and the individual surface components are mapped with few nanometer resolution. Sequentially, structural identification of the experimental reference $I(V)$ curves is achieved by comparison to theoretical reflectivity spectra calculated for distinct surface structures based on *ab initio* scattering theory. An important result from the theoretical analysis of the electron reflectivity is the striking similarity between the spectra obtained for praseodymia and ceria surfaces within the same crystal structure and oxidation state, which is explained by the almost perfect screening of the additional nuclear charge by the extra $4f$ electron in the case of praseodymia. Notably, whereas the overall oxidation state of the Pr cations is 3+, we find a non-negligible fraction of Pr^{4+} ions within a PrO_2(111)-like fluorite structure. Further distinct structural components are two novel oxygen-terminated hexagonal Pr_2O_3(0001) surface structures and a cubic, bixbyite-like Pr_2O_3(111) phase, whose relative surface coverages depend on the local step density of the substrate.

The coexistence of a variety of praseodymia crystal structures and oxidation states is expected to have important consequences for the chemical properties of the praseodymia/ruthenium system. Especially the sizeable fraction of highly oxidized Pr^{4+} species framing the oxide islands, prepared under ultrahigh vacuum conditions, should offer great potential for studying redox reactions over this interesting inverse catalytic model system using surface science techniques.

From a methodological point of view, we have demonstrated that amplitude contrast in LEEM is obtained between oxide phases varying in local stoichiometry, structure, and surface termination. Distinct surface components may be identified when combined with theoretical calculations and reference spectra acquired separately. Together with adequate experimental and established reference data, this $I(V)$-LEEM method yields the lateral distribution of the surface components of a nanoheterogeneous sample down to the lateral resolution of the microscope.

5. Acknowledgements

This research has been supported by the Institutional Strategy of the University of Bremen, funded by the German Excellence Initiative, and the Spanish Ministry of Economy and Competitiveness MINECO (Project No. FIS2016-76617-P). Furthermore, support from MAX-lab staff is kindly acknowledged.

[1] E. Bauer, Rep. Prog. Phys. 57 (1994) 895.
[2] E. Bauer, Surface Microscopy with Low Energy Electrons, Springer, 2014.
[3] J. I. Flege, E. E. Krasovskii, Phys. Status Solidi Rapid Res. Lett. 8 (2014) 463–477.
[4] I. H. Khan, J. P. Hobson, R. A. Armstrong, Phys. Rev. 129 (1963) 1513–1523.
[5] R. Zollweg, Surf. Sci. 2 (1964) 409 – 417.
[6] H.-J. Herlt, R. Feder, G. Meister, E. Bauer, Solid State Commun. 38 (1981) 973 – 976.
[7] R. Jones, P. Jennings, Surf. Sci. Rep. 9 (1988) 165 – 196.
[8] J. I. Flege, A. Meyer, J. Falta, E. E. Krasovskii, Phys. Rev. B 84 (2011) 115441.
[9] J. I. Flege, B. Kaemena, S. D. Senanayake, J. Höcker, J. T. Sadowski, J. Falta, Ultramicroscopy 130 (2013) 87–93.
[10] J. I. Flege, B. Kaemena, A. Meyer, J. Falta, S. D. Senanayake, J. T. Sadowski, R. D. Eithiraj, E. E. Krasovskii, Phys. Rev. B 88 (2013) 235428.
[11] J. Höcker, T. O. Menteş, A. Sala, A. Locatelli, T. Schmidt, J. Falta, S. D. Senanayake, J. I. Flege, Adv. Mater. Interfaces 2 (2015) 1500314.
[12] B. Santos, E. Loginova, A. Mascaraque, A. K. Schmid, K. F. McCarty, J. de la Figuera, Journal of Physics: Condensed Matter 21 (2009) 314011.
[13] M. Monti, B. Santos, A. Mascaraque, O. Rodríguez de la Fuente, M. A. Niño, T. O. Menteş, A. Locatelli, K. F. McCarty, J. F. Marco, J. de la Figuera, Phys. Rev. B 85 (2012) 020404.
[14] M. Monti, B. Santos, A. Mascaraque, O. R. de la Fuente, M. A. Niño, T. O. Menteş, A. Locatelli, K. F. McCarty, J. F. Marco, J. de la Figuera, J. Phys. Chem. C 116 (2012) 11539–11547.
[15] I. Ermanoski, G. Kellogg, Surf. Sci. 614 (2013) 1–11.
[16] E. E. Krasovskii, J. Höcker, J. Falta, J. I. Flege, J. Phys. Condens. Matter 27 (2015) 035501.
[17] J. Höcker, J.-O. Krisponeit, J. Cambeis, A. Zakharov, Y. Niu, G. Wei, L. Colombi Ciacchi, J. Falta, A. Schaefer, J. I. Flege, Phys. Chem. Chem. Phys. 19 (2017) 3480.
[18] G.-y. Adachi, N. Imanaka, Chem. Rev. 98 (1998) 1479–1514.
[19] T. E. Madey, H. A. Engelhardt, D. Menzel, Surf. Sci. 48 (1975) 304–328.
[20] J. I. Flege, J. Hrbek, P. Sutter, Phys. Rev. B 78 (2008) 165407.
[21] E. E. Krasovskii, Phys. Rev. B 70 (2004) 245322.
[22] M. Hoppe, MSc Thesis, University of Bremen, 2016.
[23] J. B. Hannon, J. Sun, K. Pohl, G. L. Kellogg, Phys. Rev. Lett. 96 (2006) 246103.